

Granular Hydrodynamics and Pattern Formation in Vertically Oscillated Granular Disks Layers

By JOSÉ A. CARRILLO¹, THORSTEN PÖSCHEL²
AND CLARA SALUÑA³

¹ICREA (Institució Catalana de Recerca i Estudis Avançats) and Departament de Matemàtiques, Universitat Autònoma de Barcelona, E-08193 Bellaterra, Spain

²Charité, Augustenburger Platz 1, 10439 Berlin, Germany

³Departament de Enginyeria Mecànica-ETSEQ, Universitat Rovira i Virgili, E-43007 Tarragona, Spain

(Received 8 September 2018 and in revised form ??)

A numerical hydrodynamic model of a vibrated granular bed in 2D is elaborated based on a highly accurate Shock Capturing scheme applied to the compressible Navier-Stokes equations for granular flow. The hydrodynamic simulation of granular flows is numerically difficult, particularly in systems where dilute and dense regions occur at the same time and interact with each other. As an example of such a problematic system we investigate the formation of Faraday waves in a 2d system which is exposed to vertical vibration in the presence of gravity. The results of the CHD agree quantitatively well with event-driven Molecular Dynamics.

1. Introduction

Recently, an interest has developed towards the hydrodynamic simulation of complex granular flows, with the aim of understanding the details of transport in the continuum limit (Goldhirsch 2003). Being both highly nonlinear and remarkably nonlocal, the mechanisms of granular transport in the dense limit are still obscure. The microscopic foundation of the hydrodynamic approaches of granular flow lies on the standard kinetic theory for molecular gases, except for the fact that dissipation is incorporated (via a constant or velocity dependent restitution) at the collision. While strictly, hydrodynamic descriptions cease to be valid near the close-packing limit, and at low restitutions, such models have however been used successfully in situations far from their supposed limits of validity, to describe for instance shock waves in granular gases (Rericha *et al.* 2002; Bougie *et al.* 2002), clustering (Hill & Mazenko 2003; Brilliantov *et al.* 2004) and coexisting phases (Meerson *et al.* 2003, 2004). The difficulty of a hydrodynamic description of granular materials has been addressed in well reasoned terms in Goldhirsch (1999, 2001). One cannot pretend to overcome the problems of such a description, however, where it works exceptionally well, one should ask how, and why.

In order to compensate for the energy lost in collisions, the typical mechanism of forcing, which is periodic vibration, induces not only the occurrence of various interesting phenomena but also the propagation of shock waves originating from the moving boundary into the system. The flow developed under these conditions is neatly supersonic and consequently, steep gradients arise in the hydrodynamic fields. For careful hydrodynamic simulations, it is then desirable to use shock-capturing methods to track the sharp fronts,

as well as high-order schemes which provide an accurate definition of the profiles. In the literature different methods have been applied to solve the Navier-Stokes equations for granular media, however, most of them lack the necessary analysis to discriminate the effects of the implicit or artificial diffusion added to handle supersonic flow.

In order to show the possibilities of state-of-the-art hydrodynamic simulations (HD) applied to granular matter, in this paper we address a paradigmatic problem of granular dynamics: the observation of Faraday waves and the quantitative description/comparison of the instability via both hydrodynamic simulations based on WENO (Weighted Essentially Non-Oscillatory) schemes and the well established method of event-driven molecular dynamics (MD). The difficulty that a hydrodynamic code faces when modeling such systems is twofold: the one introduced by the instability itself, regarding the use of proper parameters and the fine tuning of the code, and the one mentioned above, involving the propagation of shock waves across the granular bed under vibration and the discontinuities implied.

The onset of patterns in vertically oscillated granular layers has been numerically investigated via particle and hydrodynamic simulations by Bougie *et al.* (2005). The numerical scheme employed there to solve the granular Navier-Stokes equations is based upon finite differences plus artificial diffusion. In the paper a thorough analysis is done on the role of fluctuations in the pattern inception and its dependence on the acceleration parameter, and the results mainly refer to the mean square displacement of the local centre of mass of the granular layer as an order parameter. Our analysis, being also focused on the comparison between particle and hydrodynamic simulations, is concerned with the whole set of hydrodynamic aspects related to the instability and how they are reproduced in order to assess the validity of granular hydrodynamic simulations in general in complex flow problems, which is not the object of study of the mentioned paper.

The paper is organized as follows: we start in the next section summarizing the hydrodynamic description of rapid granular flows based on kinetic theory. Section 3 is devoted to explain the details of the hydrodynamic code. In Section 4 we describe the numerical hydrodynamic experiment and the molecular dynamics experiment; the results from both approaches are analyzed and compared in Section 5. In the conclusions we summarize our findings and expose a final comparison of both methods.

2. Granular Kinetic Theory and Hydrodynamics

As usual in granular kinetic theory, we follow the evolution of the number density of particles in phase space (Brilliantov & Pöschel 2004). Given a 2D granular gas composed of small homogeneous disks of diameter $\sigma > 0$ and given $(\mathbf{x}, \mathbf{V}_1)$, $(\mathbf{x} - \sigma \mathbf{n}, \mathbf{V}_2)$ the states of two particles before the collision, where $\mathbf{n} \in S^1$ is the unit vector along the disks centers, the post-collision velocities are found by assuming that a fraction of the normal relative velocity is lost while its orthogonal component is unchanged. As a consequence, the post-collision velocities are obtained as

$$\begin{aligned} \mathbf{V}'_1 &= \frac{1}{2}(\mathbf{V}_1 + \mathbf{V}_2) + \frac{\mathbf{V}'}{2} \\ \mathbf{V}'_2 &= \frac{1}{2}(\mathbf{V}_1 + \mathbf{V}_2) - \frac{\mathbf{V}'}{2} \end{aligned} \tag{2.1}$$

where $\mathbf{V}' = \mathbf{V} - (1 + e)(\mathbf{V} \cdot \mathbf{n})\mathbf{n}$, $\mathbf{V} = \mathbf{V}_1 - \mathbf{V}_2$ and $\mathbf{V}' = \mathbf{V}'_1 - \mathbf{V}'_2$, with e being the coefficient of (constant) restitution. Let us denote by \mathbf{V}_1^* and \mathbf{V}_2^* the pre-collision velocities corresponding to \mathbf{V}_1 and \mathbf{V}_2 . The Boltzmann equation for inelastic hard disks

gives the evolution of $f(t, \mathbf{x}, \mathbf{V}_1)$ and it can be written as

$$\frac{\partial f}{\partial t} + (\mathbf{V}_1 \cdot \nabla_{\mathbf{x}}) f = \sigma^2 Q(f, f) \quad (2.2)$$

where the collision operator is given by

$$Q(f, f) = G(\nu) \int_{\mathbb{R}^2} \int_{S_+^1} [(\mathbf{V}_1 - \mathbf{V}_2) \cdot \mathbf{n}] \left[\frac{1}{e} Jf(\mathbf{V}_1^*) f(\mathbf{V}_2^*) - f(\mathbf{V}_1) f(\mathbf{V}_2) \right] d\mathbf{n} d\mathbf{V}_2 \quad (2.3)$$

in which dense gas effects are taken into account through the pair correlation function $G(\nu)$, where ν is the 2D volume fraction, i.e., $\nu = \frac{\pi}{4} \rho \sigma^2$. The notation S_+^1 means that the above integral on \mathbf{n} is taking over those values of \mathbf{n} such that $((\mathbf{V}_1 - \mathbf{V}_2) \cdot \mathbf{n}) > 0$. The moments of f allow us to compute the macroscopic quantities: the number density

$$\rho(t, \mathbf{x}) = \int_{\mathbb{R}^2} f(t, \mathbf{x}, \mathbf{V}_1) d\mathbf{V}_1, \quad (2.4)$$

the velocity field

$$\mathbf{U}(t, \mathbf{x}) = \frac{1}{\rho} \int_{\mathbb{R}^2} \mathbf{V}_1 f(t, \mathbf{x}, \mathbf{V}_1) d\mathbf{V}_1, \quad (2.5)$$

and the granular temperature

$$T(t, \mathbf{x}) = \frac{1}{2\rho} \int_{\mathbb{R}^2} |\mathbf{V}_1 - \mathbf{U}(t, \mathbf{x})|^2 f(t, \mathbf{x}, \mathbf{V}_1) d\mathbf{V}_1. \quad (2.6)$$

Different formulas are proposed for $G(\nu)$ in the literature but we choose the accurate formulas obtained by Torquato (1995). More precisely, we use

$$G(\nu) = \begin{cases} \frac{1-0.436\nu}{(1-\nu)^2} & \text{for } 0 \leq \nu < \nu_f \\ \frac{1-0.436\nu_f}{(1-\nu_f)^2} \frac{\nu_c - \nu_f}{\nu_c - \nu} & \text{for } 0 \leq \nu_f \leq \nu_c \end{cases} \quad (2.7)$$

where $\nu_f = 0.69$ and $\nu_c = 0.82$ are the freezing packing fraction and the random close packing fraction respectively.

By expansion methods (Jenkins & Richman 1985*a*; Goldshtein & Shapiro 1995), the hydrodynamic equations are obtained for the 2D granular gas,

$$\begin{aligned} \frac{\partial \rho}{\partial t} + \nabla \cdot (\rho \mathbf{U}) &= 0 \\ \rho \left(\frac{\partial \mathbf{U}}{\partial t} + (\mathbf{U} \cdot \nabla) \mathbf{U} \right) &= \nabla \cdot \mathbf{P} + \rho \mathbf{F} \\ \rho \left(\frac{\partial T}{\partial t} + (\mathbf{U} \cdot \nabla) T \right) &= -\nabla \cdot \mathbf{q} + \mathbf{P} : \mathbf{E} - \gamma \end{aligned} \quad (2.8)$$

representing the evolution of the number density of particles $\rho(t, \mathbf{x})$, the velocity field $\mathbf{U}(t, \mathbf{x}) = (U_1, U_2)(t, \mathbf{x})$ and the granular temperature $T(t, \mathbf{x})$. $\mathbf{P} = (P_{ij})$ is the pressure tensor, given in terms of the tensor $\mathbf{E} = (E_{ij})$ by

$$P_{ij} = \left[-p + (2\mu_1 - \mu_2) \sum_i E_{ii} \right] \delta_{ij} + 2\mu_2 E_{ij} \quad (2.9)$$

with

$$E_{ij} = \frac{1}{2} \left(\frac{\partial U_i}{\partial x_j} + \frac{\partial U_j}{\partial x_i} \right). \quad (2.10)$$

The principal pressure is related to the density and the temperature through the equation of state

$$p = \rho\epsilon [1 + (1 + e)G(\nu)], \quad (2.11)$$

correction to the usual perfect gases law, $p = \rho\epsilon$ with $\epsilon = T$ in 2D, proposed by Jenkins & Richman (1985a); Goldshtein & Shapiro (1995); Brilliantov *et al.* (2004) to incorporate dense gas effects. The vector $\mathbf{q} = -\chi\nabla T$ models the heat flux. The viscosities μ_1 and μ_2 , the thermal conductivity χ and the cooling coefficient γ are density and temperature dependent whose explicit expression we take from Jenkins & Richman (1985a,b). The bulk viscosity is given by

$$\mu_1 = \frac{2}{\sqrt{\pi}}\rho\sigma T^{1/2}G(\nu) \quad (2.12)$$

and the shear viscosity by

$$\mu_2 = \frac{\sqrt{\pi}}{8}\rho\sigma T^{1/2} \left[\frac{1}{G(\nu)} + 2 + \left(1 + \frac{8}{\pi}\right) G(\nu) \right], \quad (2.13)$$

the thermal conductivity is

$$\chi = \frac{\sqrt{\pi}}{2}\rho\sigma T^{1/2} \left[\frac{1}{G(\nu)} + 3 + \left(\frac{9}{4} + \frac{4}{\pi}\right) G(\nu) \right] \quad (2.14)$$

and the cooling coefficient is

$$\gamma = \frac{4}{\sigma\sqrt{\pi}}(1 - e^2)\rho T^{3/2}G(\nu). \quad (2.15)$$

More involved hydrodynamic models incorporate higher order terms in the gradients expansion (Goldhirsch 2003), and more accurate expressions for the kinetic coefficients which include high density corrections (Garzó & Dufty 1999; Lutsko 2005); in principle they can be easily implemented but it is more illustrative to keep the approach as simple as possible. Finally, the vector field \mathbf{F} represents the external force acting on the system, for instance gravity modulated by the piston movement changing to the piston reference frame. The mathematical validity of the hydrodynamic approximation in the Euler case was discussed in Bobylev *et al.* (2000).

3. Details of the hydrodynamic code

In order to numerically simulate the granular Navier-Stokes equations (2.8), we write them as corrections to a compressible Euler-type system in conservation form. In fact, we consider the equivalent system

$$\begin{aligned} \frac{\partial \rho}{\partial t} + \nabla \cdot (\rho \mathbf{U}) &= 0 \\ \frac{\partial (\rho \mathbf{U})}{\partial t} + \nabla \cdot [\rho (\mathbf{U} \otimes \mathbf{U})] + \nabla p &= \nabla \cdot \mathbf{P} + \rho \mathbf{F} \\ \frac{\partial W}{\partial t} + \nabla \cdot [\mathbf{U} W] &= -\nabla \cdot \mathbf{q} + \mathbf{P} : \mathbf{E} + \mathbf{U} \cdot (\nabla \cdot \mathbf{P}) - \gamma + \rho (\mathbf{U} \cdot \mathbf{F}), \end{aligned} \quad (3.1)$$

where the total energy W is given by

$$W = \rho T + \frac{1}{2}\rho |\mathbf{U}|^2 = \rho\epsilon + \frac{1}{2}\rho |\mathbf{U}|^2. \quad (3.2)$$

The system (3.1) can be rewritten as

$$\frac{\partial \mathbf{u}}{\partial t} + \frac{\partial}{\partial x_1} \mathbf{f}(\bar{u}) + \frac{\partial}{\partial x_2} \mathbf{g}(\mathbf{u}) = \mathbf{S}(\mathbf{u}) \quad (3.3)$$

with $\mathbf{x} = (x_1, x_2)$ and obvious definitions for $\mathbf{f}(\mathbf{u})$, $\mathbf{g}(\mathbf{u})$ and $\mathbf{S}(\mathbf{u})$ and with the vector $\mathbf{u} = (u_1, u_2, u_3, u_4)$ whose components are given by

$$\begin{aligned} u_1 &= \rho \\ u_2 &= \rho U_1 \\ u_3 &= \rho U_2 \\ u_4 &= \rho \epsilon + \frac{1}{2} \rho |\mathbf{U}|^2 = \rho \epsilon + \frac{1}{2} \rho (U_1^2 + U_2^2). \end{aligned} \quad (3.4)$$

As a consequence, equations (3.1) have the structure of a system of nonlinear conservation laws with sources. Local eigenvalues and both local left- and right-eigenvectors of the Jacobian matrices $\mathbf{f}'(\mathbf{u})$ and $\mathbf{g}'(\mathbf{u})$ are explicitly computable and included in the appendix for the sake of the reader. Since local eigenvalues and eigenvectors need the derivative of the function $G(\nu)$ appearing in the equation of state (2.11), then $G(\nu)$ is smoothed out around the freezing point volume fraction ν_f .

The numerical method consists in applying a high-order shock-capturing scheme for the Euler part of this system, i.e., the left-side of (3.3), while the terms in the right-hand side $\mathbf{S}(\mathbf{u})$ are approximated by second order central finite differences.

The convective terms $\frac{\partial}{\partial x_1} \mathbf{f}(\mathbf{u})$ and $\frac{\partial}{\partial x_2} \mathbf{g}(\mathbf{u})$ are approximated by a fifth-order finite difference characteristic-wise WENO method in a uniform grid following Jiang & Shu (1996). This scheme is a well-known shock-capturing and high-order method for nonlinear conservation laws. Extensive benchmarks have shown this method to be particularly well adapted to control oscillations in shock regimes in classical Euler equations for gases, see the survey by Shu (1998).

We first restrict ourselves to the one dimensional procedure, working in a dimension-by-dimension fashion for reconstructing each of the fluxes in Eq. (3.3). This means that when approximating $\frac{\partial}{\partial x_1}(\mathbf{f}(\mathbf{u}))$, for example, the other variable x_2 is fixed and the approximation is performed along the x_1 line. Given a uniform grid r_i for any of the spatial variables denoted by r , let us call $\mathbf{u}_i(t)$ the numerical approximation to the point value $\mathbf{u}(r_i, t)$. The corresponding convective term is approximated as

$$\frac{\partial}{\partial r} \mathbf{f}(\mathbf{u}) \simeq \frac{\hat{\mathbf{f}}_{i+\frac{1}{2}} - \hat{\mathbf{f}}_{i-\frac{1}{2}}}{\Delta r} \quad (3.5)$$

where $\hat{\mathbf{f}}_{i+\frac{1}{2}}$ is the numerical flux.

Let us briefly describe the general characteristic-wise finite difference procedure with flux splitting and flux reconstruction. At each fixed time t , we find the numerical fluxes $\hat{\mathbf{f}}_{i+\frac{1}{2}}$ in the following way:

Step 1. We first compute an average or intermediate state $\mathbf{u}_{i+\frac{1}{2}}$ using Roe's formula as in Shu (1998); Kamenetsky *et al.* (2000).

Step 2. We compute the matrices of right \mathbf{R} and left \mathbf{R}^{-1} eigenvectors and eigenvalues $\Lambda_l(\mathbf{u}_{i+\frac{1}{2}})$, $l = 1, \dots, 4$, of the Jacobian matrix $\mathbf{f}'(\mathbf{u}_{i+\frac{1}{2}})$ from the formulas postponed

to the appendix to obtain

$$\begin{aligned}\mathbf{R} &= \mathbf{R}\left(\mathbf{u}_{i+\frac{1}{2}}\right) \\ \mathbf{R}^{-1} &= \mathbf{R}^{-1}\left(\mathbf{u}_{i+\frac{1}{2}}\right) \\ \mathbf{\Lambda} &= \mathbf{\Lambda}\left(\mathbf{u}_{i+\frac{1}{2}}\right) = \text{diag}\left[\Lambda_l\left(\mathbf{u}_{i+\frac{1}{2}}\right)\right].\end{aligned}\tag{3.6}$$

Step 3. We transform the values \mathbf{u}_i and $\mathbf{f}(\mathbf{u}_i)$ in the potential stencil of the approximation of the flux to the local characteristic coordinates by using the left eigenvectors:

$$\mathbf{v}_i = \mathbf{R}^{-1}\mathbf{u}_i \quad \text{and} \quad \mathbf{h}_i = \mathbf{R}^{-1}\mathbf{f}(\mathbf{u}_i).\tag{3.7}$$

Step 4. We use global Lax-Friedrichs flux splitting with the transport coefficient computed from the maximum, in absolute value, among the above computed eigenvalues to get \mathbf{h}_i^\pm from

$$\mathbf{h}_i^\pm = \frac{1}{2}(\mathbf{h}_i \pm \alpha \mathbf{v}_i),\tag{3.8}$$

where the dissipation parameter α is given by

$$\alpha = \max_{i,l} \left| \Lambda_l\left(\mathbf{u}_{i+\frac{1}{2}}\right) \right|.\tag{3.9}$$

Step 5. We compute the decomposed fluxes $\hat{\mathbf{h}}_{i+\frac{1}{2}}^+$ and $\hat{\mathbf{h}}_{i+\frac{1}{2}}^-$ at the middle points using a high-order reconstruction explained below.

Step 6. We transform back the computed fluxes to the physical space by using the right eigenvectors

$$\hat{\mathbf{f}}_{i+\frac{1}{2}}^\pm = \mathbf{R}\hat{\mathbf{h}}_{i+\frac{1}{2}}^\pm\tag{3.10}$$

and finally, we add them to obtain the final numerical flux

$$\hat{\mathbf{f}}_{i+\frac{1}{2}} = \hat{\mathbf{f}}_{i+\frac{1}{2}}^+ + \hat{\mathbf{f}}_{i+\frac{1}{2}}^-.\tag{3.11}$$

Instead of Roe mean and Lax-Friedrichs flux splitting formulas, we can use more sophisticated and improved methods avoiding numerical diffusion but in this case we do not need them since Navier-Stokes terms will have a regularizing effect anyhow on shock waves in the flow.

In the WENO5 method, reconstructions of the fluxes in Step 5 are done using a non-linear nonlocal convex combination of three different approximations of the flux by three different local stencils using the upwinding of the flux. The contribution of each approximation for the computation of the final value of the flux depend on the local smoothness of the function measured by certain smoothness indicators based on the local divided differences. If the function is smooth the resulting approximation is fifth order. The idea behind this weighted approximation is that those stencils including a discontinuity or high gradient will receive almost zero weight in the approximation and thus, oscillations will be avoided while keeping high-order approximation in smooth parts of the flow.

More precisely, let us denote by $\hat{h}_{i+1/2,l}^+$ the l -th component of the local numerical flux $\hat{\mathbf{h}}_{i+1/2}^+$ and by $h_{i,l}^+$ the l -th component of the local flux \mathbf{h}_i^+ . Since the computations below are analogous component by component and fixed for the chosen upwinding, we will avoid the sub- and superindex ^+_l for notational simplicity. Then, we obtain the numerical flux $\hat{h}_{i+1/2}$ by

$$\hat{h}_{i+1/2} = \omega_1 \hat{h}_{i+1/2}^{(1)} + \omega_2 \hat{h}_{i+1/2}^{(2)} + \omega_3 \hat{h}_{i+1/2}^{(3)}\tag{3.12}$$

where $\hat{h}_{i+1/2}^{(m)}$ are the three third order fluxes on three different stencils given by

$$\begin{aligned}\hat{h}_{i+1/2}^{(1)} &= \frac{1}{3}h_{i-2} - \frac{7}{6}h_{i-1} + \frac{11}{6}h_i, \\ \hat{h}_{i+1/2}^{(2)} &= -\frac{1}{6}h_{i-1} + \frac{5}{6}h_i + \frac{1}{3}h_{i+1}, \\ \hat{h}_{i+1/2}^{(3)} &= \frac{1}{3}h_i + \frac{5}{6}h_{i+1} - \frac{1}{6}h_{i+2},\end{aligned}\tag{3.13}$$

and the nonlinear weights ω_m are given by

$$\begin{aligned}\omega_m &= \frac{\tilde{\omega}_m}{\sum_{l=1}^3 \tilde{\omega}_l} \\ \tilde{\omega}_l &= \frac{\gamma_l}{(\varepsilon + \beta_l)^2}\end{aligned}\tag{3.14}$$

with the linear weights γ_l given by

$$\gamma_1 = \frac{1}{10}, \quad \gamma_2 = \frac{3}{5}, \quad \gamma_3 = \frac{3}{10},\tag{3.15}$$

and the smoothness indicators β_l given by

$$\begin{aligned}\beta_1 &= \frac{13}{12}(h_{i-2} - 2h_{i-1} + h_i)^2 + \frac{1}{4}(h_{i-2} - 4h_{i-1} + 3h_i)^2 \\ \beta_2 &= \frac{13}{12}(h_{i-1} - 2h_i + h_{i+1})^2 + \frac{1}{4}(h_{i-1} - h_{i+1})^2 \\ \beta_3 &= \frac{13}{12}(h_i - 2h_{i+1} + h_{i+2})^2 + \frac{1}{4}(3h_i - 4h_{i+1} + h_{i+2})^2.\end{aligned}\tag{3.16}$$

Finally, ε is a parameter to avoid the denominator to become 0 and is taken as $\varepsilon = 10^{-6}$ in the computation of this paper. The computation for approximating $\hat{\mathbf{h}}_{i+1/2}^-$ is obtained with the alternate upwinding by mirror symmetry with respect to the index $i + \frac{1}{2}$. We refer to the survey by Shu (1998) for further details about WENO reconstruction procedures, smoothness indicators, benchmarks and references for different applications.

Finally, the resulting ODE system is solved in time by a 3rd-order TVD Runge-Kutta scheme introduced by Shu & Osher (1998) imposing a local CFL condition at every time step, ensuring that the numerical speed is not less than the the largest eigenvalue of the local Jacobian matrix. This CFL condition becomes more restrictive as we approach the close-packing volume fraction. Although viscosity and thermal conductivity terms are treated as sources, they are taken into account in the CFL condition since diffusion effectively paces the time stepping of the code. This fact is due to the dependence of the viscosity and thermal conductivity on the volume fraction, resulting in diverging coefficients for both close-packing and vacuum limits. Both limits are avoided in the actual computation shown in this paper by establishing a limit from above and below of the volume fraction. These limits are 10^{-4} and 99.99% of the maximal volume fraction.

4. Numerical experiments

4.1. Structures in vertically oscillated granular systems

When granular matter is exposed to vertical oscillations in the presence of gravity, one observes spatio-temporal structures at the free surface. Although this observation was reported as early as 1831 by Faraday the effect was studied only in recent years systematically and a variety of patterns was observed, e.g. by Pak & Behringer (1993);

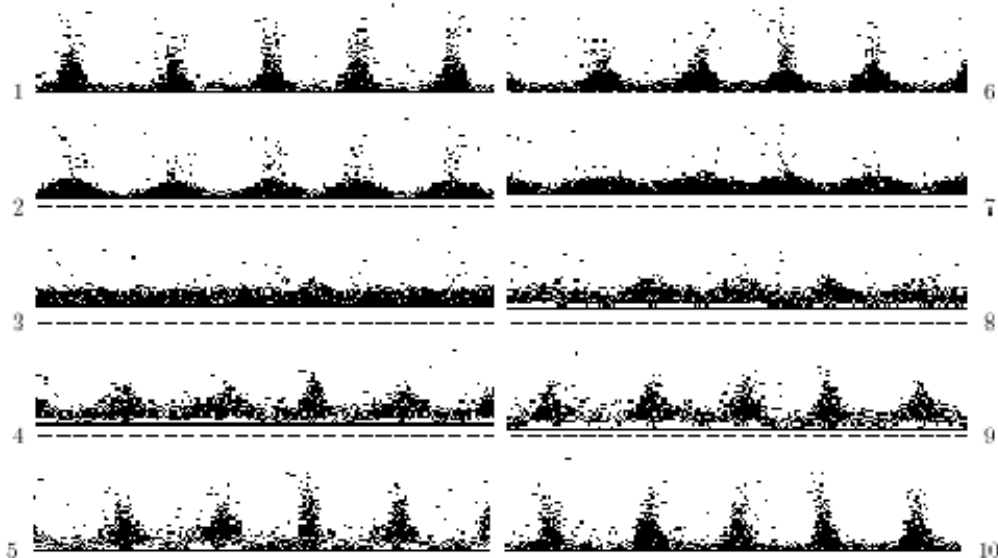


FIGURE 1. Periodic wave-like pattern in a vertically vibrated granular layer. The period of the pattern is twice the period of the excitation. The figure shows a two-dimensional MD simulation of 3000 particles at $A = 4.02$, $f = 3.5$ (details see below). Only a part of the system is shown. The dashed line indicates the lower amplitude of the oscillation. An animated sequence is provided as supplementary material.

van Doorn & Behringer (1997); Melo *et al.* (1994, 1995); Umbanhowar *et al.* (1996, 1998); Metcalfe *et al.* (1997) and theoretically explained, e.g., by Rothman (1998); Tsimring & Aranson (1997).

Here we focus on subharmonic instabilities in a vertically vibrated layer of granular matter, first reported by Douady *et al.* (1989) and further characterized in dependence on the parameters of the vibration by Clément *et al.* (1996); Wassgren *et al.* (1996). Above a certain amplitude of acceleration, $\Gamma = A\omega^2/g$ (A is the amplitude, ω the frequency of the sinusoidal excitation, g is gravity), a periodic wave-like pattern appears with frequency $\omega/2$. Although the condition $\Gamma > 1$ is not a necessary condition for pattern formation (Pöschel *et al.* 2000; Renard *et al.* 2001), in all experimental observations the onset of the pattern formation was observed for $\Gamma \gtrsim 4$.

These waves could be reproduced in quantitative agreement with experiments by numerical MD simulations by Luding *et al.* (1996); Luding (1997) and by Aoki & Akiyama (1996) (see also Bizon *et al.* 1997; Aoki & Akiyama 1997) and were also found from a linear stability analysis of an oscillating granular layer, modeled as an isothermal incompressible fluid with vanishing surface tension (Bizon *et al.* 1999). Figure 1 shows snapshots of a Molecular Dynamics simulation.

A computational fluid mechanics simulation of such a system represents a hard problem since the granular material occurs in dense state (e.g. snapshots 2 and 3 in Figure 1) and in dilute state (e.g. snapshots 4 and 9 in Figure 1). A universal CFD computation should be capable to describe the system in both states dense and dilute.

The described effect and its dependence on the system parameters was well studied in the literature; in the present paper it serves as an example showing that our CFD simulation is in quantitative agreement with MD simulations and, thus, capable to describe time-dependent behavior of granular systems in dense and dilute state. For simplicity

and better visual representation, here we restrict ourselves to a two-dimensional system, the generalization to 3D is conceptually simple although computationally expensive.

4.2. Setup of the Molecular Dynamics system

Our reference system is an event-driven Molecular Dynamics simulation as shown in Figure 1. In event-driven MD, each of the N particles of the system moves along a parabolic trajectory due to gravity g . This motion is interrupted by binary collisions, where each of the collision partners changes its velocity according to Eq. (2.1). Given particle positions and velocity at time t , the time of the next collision in the entire system can be computed analytically, therefore, in event-driven simulations, the time progresses in irregular steps, from event to event, i.e., from collision to the next collision. Unlike force-based MD, where Newton's equation of motion is solved numerically by evaluating the interaction forces, event-driven MD does not solve Newton's equation explicitly. Instead, Newton's equation is implied in the coefficient of restitution which relates the relative particle velocity after a collision to the velocity before the collision, Eq. (2.1), that is, the coefficient of restitution itself which, in general, is a function of material parameters and impact velocity, is a result of solving Newton's equation (Brilliantov *et al.* 1996; Schwager & Pöschel 1998; Ramírez *et al.* 1999). In the present paper, we assume that the coefficient of restitution is a material constant and adopts the value $e = 0.75$.

The main precondition for applying event-driven MD is the assumption of binary collisions which implies hard particles. Although conceptually simple, an efficient implementation of event-driven MD algorithms is by far more complex than force-based algorithms (see, e.g., Pöschel & Schwager 2005). To compare particle dynamics with hydrodynamics, it is necessary to employ event-driven MD since both MD and HD simulations are based on the same equations (2.1) using both the concept of binary collisions and the coefficient of restitution. In general, there is no simple correspondence between force-based MD and hydrodynamics.

The disadvantage of event-driven MD is its restriction to binary and thus, instantaneous collisions. While for dilute granular gases this assumption is well justified, for systems with gravity, for mathematical reasons we cannot exclude tree-particle interaction, also called *inelastic collapse* (McNamara & Young 1993). There are numerical tricks to avoid or retard the inelastic collapse in MD simulations (e.g., Luding & McNamara 1998), provided density is small enough, however, for systems with gravity and reflecting oscillating bottom wall, at low frequency event-driven simulations become problematic: Consider a ball falling vertically from a certain height. At each collision with the wall its energy is reduced by the factor e^2 . Then, in *finite* time the ball comes to rest, that is, it stays in permanent contact with the wall which violates the condition of instantaneous contacts. The same argument applies for slowly oscillating walls, therefore, our simulations fail for low oscillation frequency.

To compare event-driven simulations with CFD results, we perform simulations of an assembly of N particles of diameter $\sigma = 10$ mm, colliding due to Eq. (2.1) with coefficient of restitution $e = 0.75$. The width of the system is L . After the transient time when the pattern is time-invariant (except for its period), we recorded the horizontal positions of all particles for 50 periods. The number of peaks N_p of this pattern was then determined by visually inspecting the histogram of this data. In addition, we determined the wave lengths λ of the pattern by Fourier-analysis, which agrees well with the values for N_p .

Table 1 shows the parameters of the performed event-driven MD simulations and the results for N_p and λ , extracted from Fourier analysis. The standard deviations $d\lambda$ account for the spread of the wavelength, which at very low amplitudes / accelerations is specially

TABLE 1. Performed MD simulations. N – number of particles, $f = 2\pi\omega$ – frequency of the oscillating bottom wall (in Hz), A – amplitude of the oscillation, L – system width, H – number of particle layers. The observed patterns are characterized by N_p – number of peaks, λ – wave length, $d\lambda$ – standard deviation of the measured wavelength over 50 cycles. All lengths are given in units of the particle diameter.

Γ	N	f	A	L	H	N_p	λ	$d\lambda$
2.00	1879	5.5	1.64	300	6	15	18	21
2.00	2506	5.0	1.99	400	6	16	25	18
2.00	2506	4.5	2.45	400	6	13	31	18
2.00	2506	4.0	3.12	400	6	11	37	15
2.00	3132	3.5	4.02	500	6	12	42	5
2.00	3759	3.0	5.50	600	6	12	50	10
2.25	1566	6.0	1.55	250	6	12	21	9
2.25	1879	5.5	1.85	300	6	13	23	7
2.25	2506	5.0	2.24	400	6	15	27	4.5
2.25	2506	4.5	2.76	400	6	14	29	4.5
2.25	3759	4.0	3.51	600	6	19	31	2
2.25	3759	3.5	4.52	600	6	14	43	7
2.25	3759	3.0	6.19	600	6	12	50	13
2.52	1880	5.5	2.07	300	6	15	20	9
2.52	1880	5.0	2.50	300	6	12	25	7
2.52	1880	4.5	3.09	300	6	11	27	6
2.52	1880	4.0	3.90	300	6	9	33	6
2.52	3132	3.5	5.07	500	6	12	42	7
2.52	3132	3.0	6.92	500	6	10	50	16
2.75	3132	3.5	5.57	500	6	13	39	8
2.75	3132	3.0	7.59	500	6	9	56	13
2.75	3759	2.5	10.9	600	6	9	67	15

high. The range of amplitudes A and accelerations Γ investigated is devised to capture the development of the instability; the width of the system L is chosen to ensure that a sufficient number of wavelengths fits the simulation window – and thus the errors in the determination of λ are diminished. These results will be discussed below in Sec. 5 in comparison with the results of the computational hydrodynamics.

Hydrodynamic fields such as density, velocity and temperature were generated from 50 cycles of the MD simulation at amplitude $A = 5.6\sigma$ (σ : particle diameter) and frequency $f = 3.5$ Hz, with the aim to compare them with the respective fields from the HD simulation. For this purpose we used a $150\sigma \times 50\sigma$ grid. The positions and velocities of all particles were recorded for 50 periods at a rate of 50 fixed equidistant phases per period. In order to generate hydrodynamic fields, phase averaging was performed over particle positions and velocities with a spatial coarsegraining function (Goldhirsch 1999) $\phi(\mathbf{r}) \propto \theta(\sigma/2 - |\mathbf{r} - \mathbf{r}_i(t)|)$ where θ is the Heaviside step function and $\mathbf{r}_i(t)$ the instantaneous location of the center of a particle. The cell size for averaging fits about 3×1 particles, which leaves us with a typically mesoscopic procedure.

4.3. Setup for the hydrodynamic system

We solve the full set of equations in 2D (2.8) supplied with the kinetic coefficients given by Eqs. (2.12)-(2.15) and the equation of state (2.11) on a $150 \times (50 \text{ up to } 100)$ rectangular grid. The initial state is prepared by leaving the material settle down under the action of gravity to form a deposited layer of 6 grains. The depth of the granular bed is imposed by assuming a close random packing density in the deposited layer. As in MD simulations, the diameter of the grains is $\sigma = 10 \text{ mm}$ and their restitution $e = 0.75$.

The domain in which the hydrodynamic equations are solved varies in the range of 300 to 600σ along the x_1 direction, and from 30 to 100σ along the vertical or x_2 direction for the range of amplitudes A and frequencies f sampled in the simulations (1.5 to 15σ in amplitude, 2 to 6 Hz in frequency). This way we make sure that the scale of the pattern is correctly modeled and a sufficient number of pattern wavelengths is captured. The choice of the vibration parameters is adjusted to cover the bifurcation region, that is, the region where the granular layer destabilizes from the homogeneous (along the x_1 direction) solution. In general, we use exactly the same values for the parameters as in the MD simulations.

We use periodic boundary conditions along the x_1 direction, while at the top and the bottom we set reflecting boundaries. The top wall is set at a distance where reflections are of minor importance (the packing fraction at those heights is always of the order of 10^{-4}). The hydrodynamic fields (density, velocity components, temperature) are stored for subsequent inspection without any additional treatment. Since the homogeneous solution tends to be very stable in the absence of random sources, we numerically perturb the layer density with a collection of modes (the first 20 with largest wavelengths), with random phases and amplitudes. The latter are selected with a maximum in the order of 10^{-3} times the value of the local packing fraction of the deposited material. This small perturbation is sufficient to quickly observe the growth of the mode selected by the system which gives rise to the development of the Faraday waves (see supplementary material).

5. Results

Unlike particle simulations, in hydrodynamic simulations the patterns tend to be very stable and regular for small as well as for moderate amplitudes. The growth of the selected wavelength develops within 10 cycles after the perturbation has been imposed (see supplementary material), and one observes only minor changes after this time. The periodicity of the pattern is twice the shaking period, as corresponds to the typical period doubling of this instability. Figure 2 shows the appearance of the pattern in a sequence of eight frames which covers two periods of shaking and the corresponding frames generated from the MD simulation.

The main difference between the HD and MD sequences in Figure 2 is the different landing time of the granular bed. The fourth and the eighth snapshots are taken when the material visibly starts to deposit, which happens at different times in HD and MD simulations. This deserves a careful discussion. Indeed, one of the typical features accompanying the instability is the gap formed between the material and the bottom wall, induced by an acceleration of the plate at $\Gamma > 1$. In real experiments as well as in MD simulations – and leaving aside the effects of particle noise, there is a true empty space opening and closing periodically. In HD simulations the density is never very close to zero at the bottom wall. This fact has to be attributed to the implemented boundary condition. More will be said in this respect later in this section.

The bifurcation diagram is shown in Figure 3, from which one can easily observe the

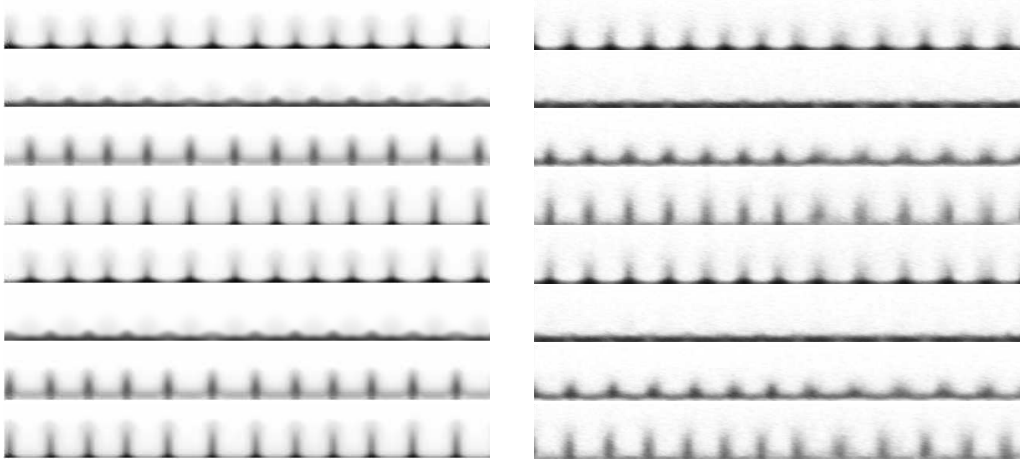


FIGURE 2. Eight pictures of the density as obtained from the numerical solution of the hydrodynamic equations (HD, left) and the corresponding ones from the molecular dynamics simulation (MD, right). The times for the HD snapshots are: $0, 0.25T, 0.5T, 0.75T, T, 1.25T, 1.5T, 1.75T$, with T being the period of the oscillation. The MD snapshots were taken at times: $0, 0.25T, 0.5T, T, 1.25T, 1.5T, 1.86T$. The initial phase is arbitrary, but common for both sets. For most of the period, the dynamics observed in HD and MD simulations is completely equivalent; the difference in the fourth and eighth phases is due to different landing times of the granular bed (see text). The MD figures are obtained after averaging particle positions over 50 cycles, while the density field on the left is the raw output. The frequency of vibration is $f = 3.5$ Hz and the amplitude $A = 5.6$ diameters. Complete sequences are available as supplementary material.

extent of the agreement that both types of simulations can provide, with results which quantitatively diverge by no more than 20%. Close to the bifurcation point though, there is an important exception: According to the hydrodynamic simulations, the pattern starts to form between 1.55 and 1.64 diameters of amplitude, since below $A = 1.64\sigma$ it is not observed for any reduced acceleration $\Gamma = A(2\pi f)^2/g$ in the range from 2.0 to 2.75, where g is the acceleration of gravity. For the MD simulations, however, one obtains a few data points in the region of very low amplitudes giving nonzero wavelengths. Nevertheless the errors associated with these few MD measures are particularly large, coming from the procedure to determine the characteristic pattern wavelength in MD simulations: due to the general contribution of particle noise, the wavelength was extracted from the histogram of the Fourier analysis of the particle positions over 50 periods. Otherwise, in the low amplitude regime, no pattern would be guessed from the naked-eye inspection of the MD sequences. Therefore, the typical histograms contain a wide spread of wavelengths in this regime, which reflects in the standard deviations ($d\lambda$ in Table 1) plotted in Figure 3 as error bars. The duplicate data points in some of the hydrodynamic samples refer to situations where a child peak develops or disappears (due to finite size effects introduced by the periodic boundaries) and as a result, both wavelengths can be observed in the course of one simulation. This tends to happen in the large amplitude regime, where the pattern is less stable.

In Figure 4 we show a 2-period sequence of the vertical profiles of the packing fraction ν and the rescaled internal energy $\rho T/\sigma g$, as a function of height in diameters. For the plots we have selected one of the locations in Figure 2 where a valley/cusp develops alternatively. The first snapshot (a) shows the granular material already being compressed by the incoming bottom wall. As one can appreciate, the extent of the layer (solid line) is small so the profile corresponds to the location of a valley at this time. The thermal

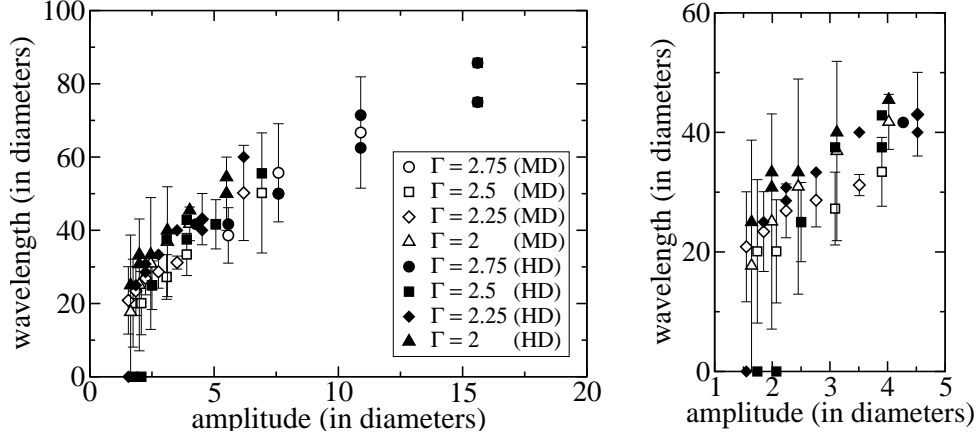


FIGURE 3. The wavelength of the pattern as a function of the amplitude of shaking, for different reduced accelerations Γ . Open symbols: Numerical solution of the hydrodynamic equations; full symbols: Event-driven molecular dynamics simulations. On the right: A zoom of the figure at low amplitudes. Error bars are drawn only for MD data points.

energy is high and has started to propagate upwards after the impact. In Figure 4(b) the layer is thickening while at the peaks is thinning, as (f) shows. In (c) the energy has already propagated to the top, the material is suspended and rather fluidized, and the cusp is visible. In (d) another impact is taking place, the density is growing at the bottom, and one more shock wave has been generated whose energy extincts as the peak redissolves to feed the closest locations where new cusps are forming – indeed, in (e) the material is close packed at the bottom, and thus density can only further decrease by pressure gradients. From the comparison between (c) and (g), one can see that the densities are very different in peaks and valleys, and the shock progresses thus differently. The careful analysis of the shock wave propagating through a (homogeneous) vibrated bed has been done by Bougie *et al.* (2002) and here suffices to point at the fact that the flow is indeed supersonic, with Mach numbers in the range from 0 to 10. See the Figure 5 to observe the typical oscillations of the Mach number at a valley / cusp. The highest values of the Mach number are achieved in the dilute phase but not far away from the clustered phase; the figure shows the Mach number recorded at the height where the packing fraction is 5%, as a convenient measure of the interface between the dense and rarefied material. The convective motion along the x_1 direction which removes material from the dense towards the dilute locations will be analyzed later.

For the MD simulation, the time-dependent thermal energy has been extracted by averaging over 50 cycles the corresponding phases of the local fluctuational kinetic energy, as defined by Eq. (2.6). Afterwards an average over equivalent locations has been performed. The profiles are shown in Figure 6. Comparison between Figs. 4 and 6 indicates that the quantitative difference in the temperature profiles is small. However, the hydrodynamic profiles show a sharper shock wave, as compared with their corresponding MD counterparts. This feature is related to the residual heating observed in MD simulations at heights where the granular layer is sufficiently dilute (very visible for example in Figure 6f). Movies showing the complete sequences are available as (supplementary material). From their inspection one can realize that the maximum values of the temperature do not

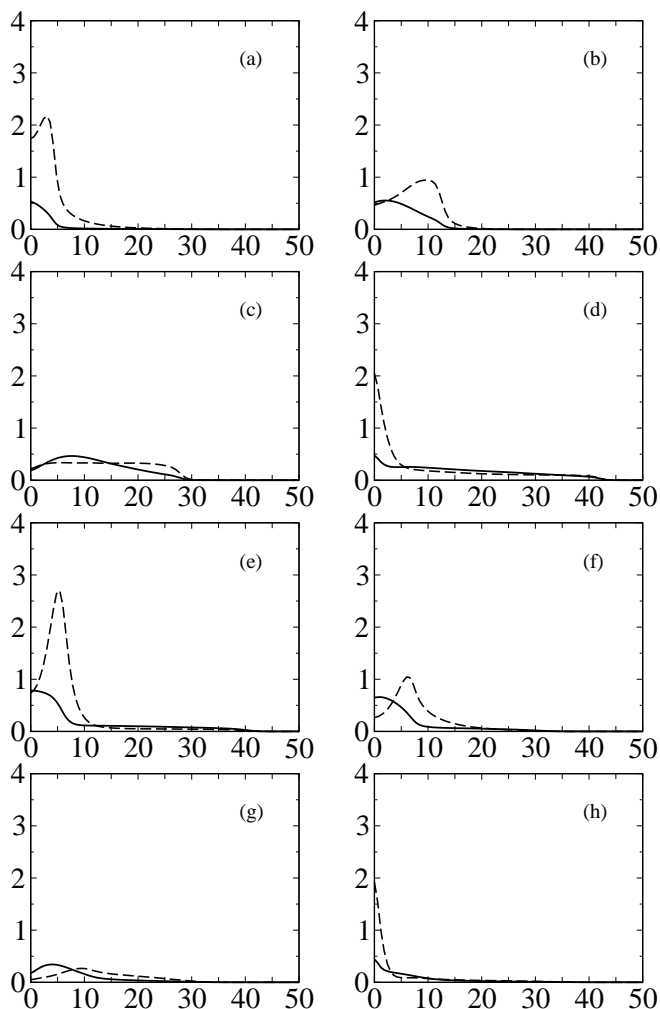


FIGURE 4. Hydrodynamic simulation: A 2-period sequence of the vertical profiles of the packing fraction ν (solid line) and the rescaled internal energy $\rho T/\sigma g$ (dashed) as a function of height, in diameters, for the same times as the snapshots in Figure 2(left).

differ very significantly, whereas the MD profiles appear systematically thicker. This phenomenon might be attributed in part to the mesoscopic averaging procedure employed here. It is certainly known, on the other hand, that hydrodynamic variables can be scale dependent in granular systems (Goldhirsch 2001) due to the lack of scale separation. So even if the number of samples (cycles) could in principle be increased, and therefore the mean fields better defined, the local noise will persist at scales of the order of one particle (which is the grid size used here for averaging the MD sequences), particularly in dilute regions. The number of samples is practically limited by the fact that the MD pattern is not strictly stationary for very long times. It is not desirable either to increase the grid size for averaging, for obvious reasons: Here, where the pattern is of the size of a few grains, the fields obtained from MD simulations would lose structure and definition. Oppositely, the granular Navier-Stokes equations (2.8) do not account for such a source of fluctuations. However, and even with these restrictions, one can conclude that good quantitative agreement can be achieved with mesoscopic statistics: a manageable number

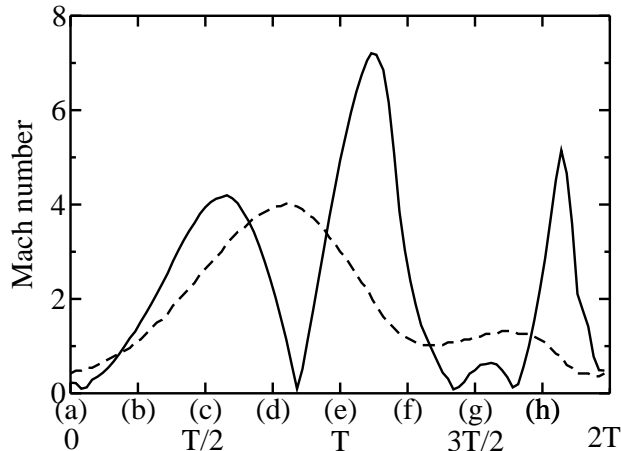


FIGURE 5. Solid line: Evolution of the Mach number over two periods for the frames in Figure 4 at a height (variable) where the packing fraction is 5%. Dashed line: height (in diameters divided by 10) corresponding to the values of the Mach shown.

of samples (25) and a one-diameter characteristic cell size, along with a final average of means over corresponding locations.

There is still another difference between the MD and HD profiles, and it is related to the gap formed when the granular layer takes off (Figure 2c and g). In MD simulations, during the stage of downward displacement of the wall, the entire layer is levitating, as one can observe from the corresponding frames in Fig. 6 by noting that the density at zero height is exactly zero. However, in HD simulations the density at the bottom is never very close to zero. It is particularly large at the base of the cusps, (Figure 4c), where the packing fraction is 0.19. Seemingly, the hydrodynamic layer is more sticky, or behaves more inelastically, than the MD granular bed. Besides that, in hydrodynamic simulations, the fact that there is some material stuck to the bottom during the take off anticipates the impact with the wall and the corresponding generation of the shock wave. This is the source of the mismatch between the landing times, to which Figure 2 refers.

It is worth to analyze the velocity field and the convection pattern which accompanies the Faraday waves. These are shown in values relative to the velocity of the plate in Figs. 7 and 8 for hydrodynamic and MD simulations, respectively, and in the supplementary material. In fact what is shown is the linear momentum field rather than the velocity, in order to focus onto the most relevant part of the system eliminating from the picture the almost empty regions. Comparing both panels we see again the effect that was pointed at above: in hydrodynamic simulations, the material never abandons contact with the vibrating plate. This feature has been observed before in hydrodynamic simulations of vibrated granular layers without pattern formation (Shattuck 2005). Besides that, in Figs. 7 and 8 we observe the removal of material from the dense towards the loose regions after each impact of the wall, during the alternate formation of cusps. The scaling factor for the arrows – chosen identical for both figures, again reveal good quantitative agreement of the hydrodynamic simulations and MD. In HD we obtain slightly lower values of the linear momentum as compared with MD simulations, by a factor which is shown to be about 20% – the maximum value achieved by the linear momentum was 1.17 in some units for the MD sequence; for the HD simulation was 0.935. We recall that simple reflecting boundaries are used for the hydrodynamic simulations (with zero no-slip), and that particles are perfectly smooth in MD simulations. It is difficult to evaluate the

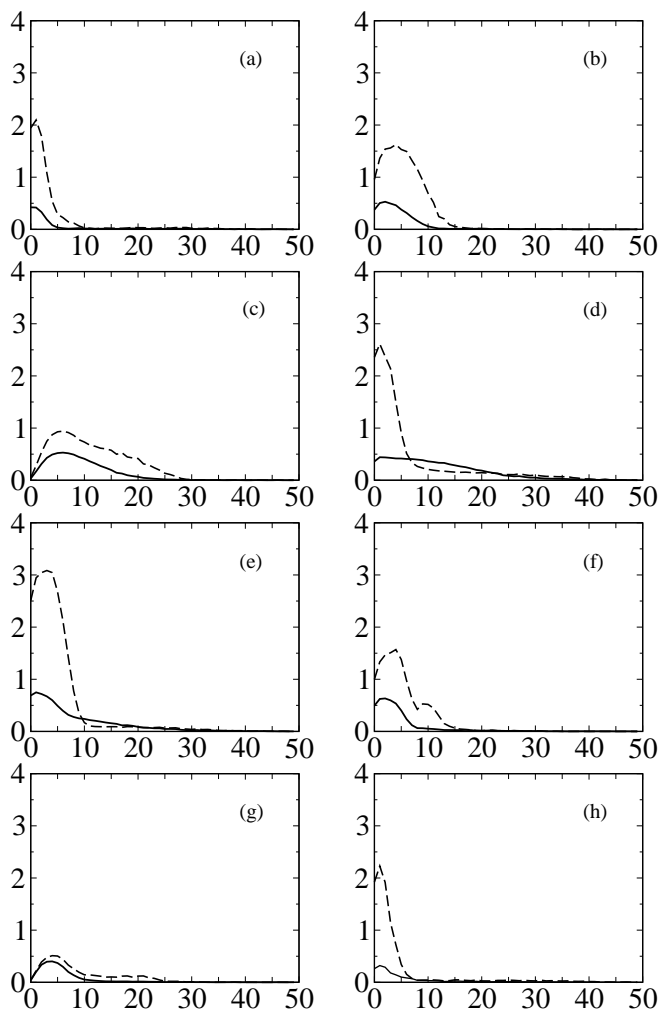


FIGURE 6. Molecular Dynamics simulation: A 2-period sequence of the vertical profiles of the packing fraction ν (solid line) and the rescaled internal energy $\rho T / \sigma g$ (dashed) as a function of height, in diameters, for the same times as the snapshots in Figure 2(right).

effect of the choice of boundary conditions in more complex setups, but in view of the results, it seems clear that this undisturbed sliding along the plate looks like the only reasonable choice in this very simple situation.

6. Conclusions

Up to now, we have compared the results given by the two simulation methods considered: The traditional approach by event-driven MD and the hydrodynamic approach by means of a CFD code. We have shown that qualitatively and quantitatively as well, adequately armored hydrodynamic codes can reproduce the features of particle simulations in complex flow problems dealing with transient strong shock waves and pattern formation, such as the Faraday instability here investigated. In particular, the appearance and wavelength of the pattern has been reproduced with a very good approximation as seen from the bifurcation diagram (Figure 3). The hydrodynamic fields compare very

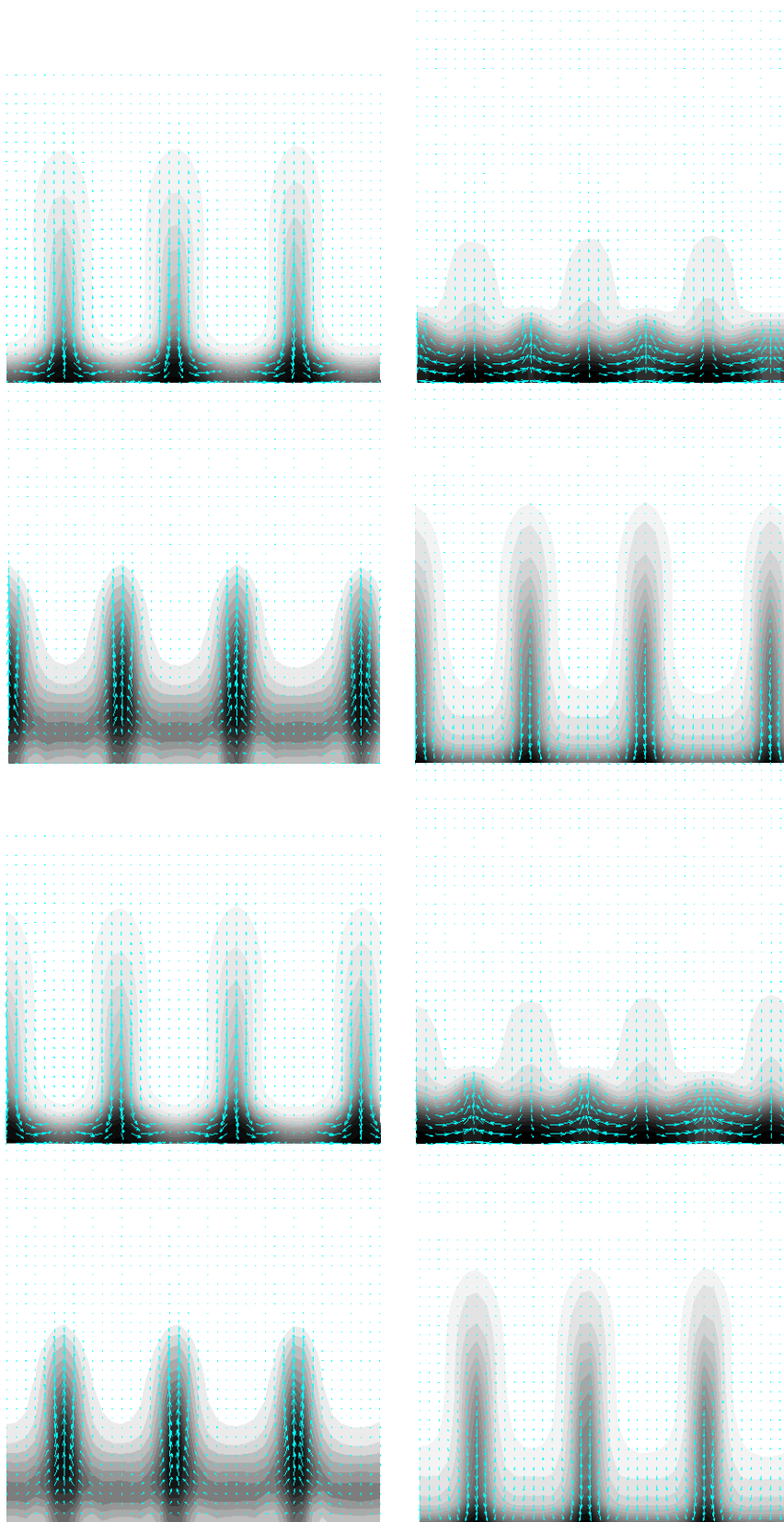


FIGURE 7. Hydrodynamic simulation: The linear momentum plotted over the density field in gray shades. The frames are taken at the same times as in Figure 2(left) and cover two cycles of the driving oscillation. The complete sequence is available as supplementary material.

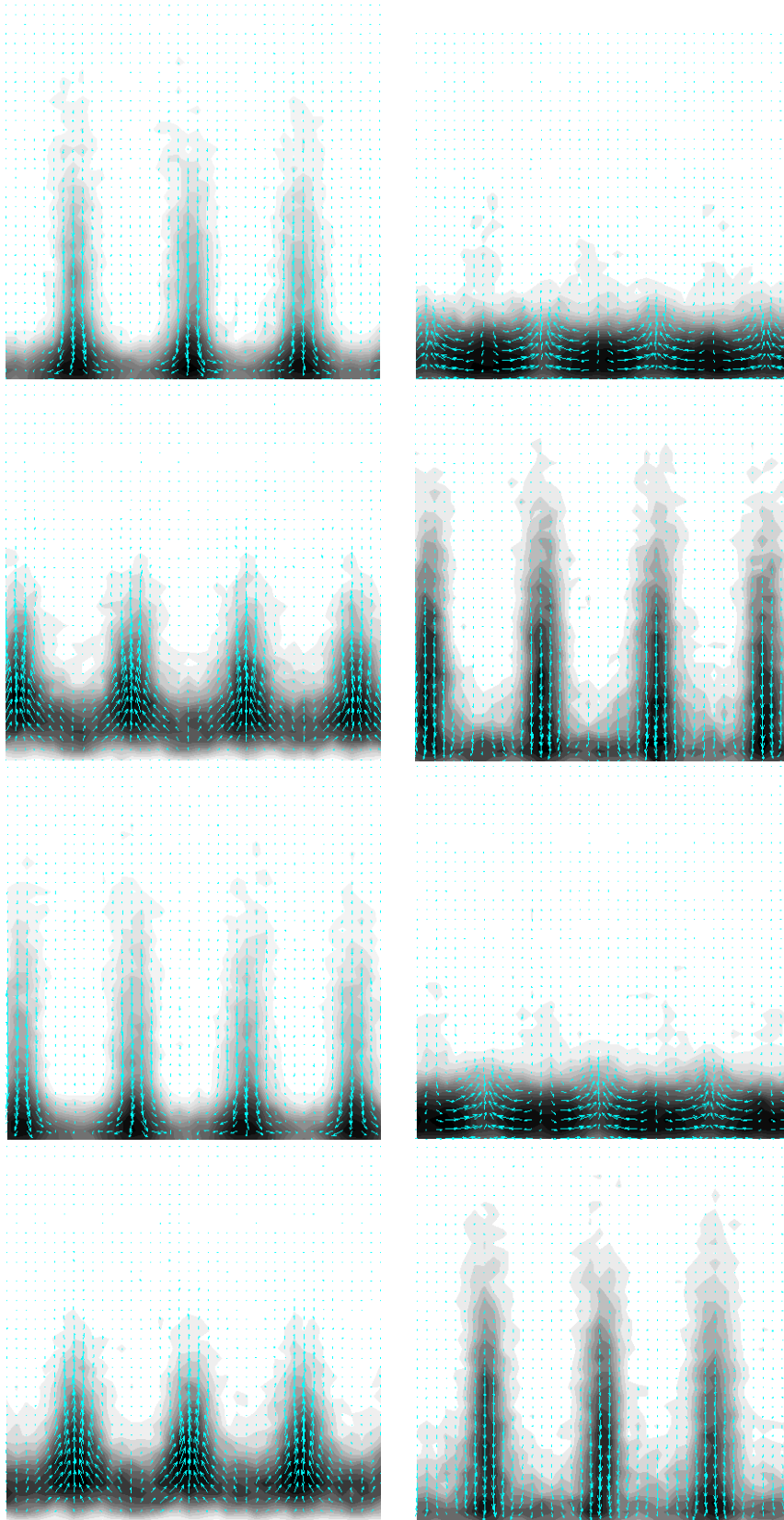


FIGURE 8. Molecular Dynamics simulation: The linear momentum plotted over the density field in gray shades. The frames are taken at the same times in Figure 2(right) and cover two cycles of the driving oscillation.

well to the corresponding averaged particle fields (with the exception of the gap formed during the take off of the granular layer). The hydrodynamic temperature is shown to agree with its MD counterpart to which ensemble averaging at a typical grid size of one particle diameter has been applied. Last, the velocity field obtained in hydrodynamic simulations follows the periodic alternancy of the pattern and shares the type of structure observed in the particle velocity field, if however giving somewhat smaller values. The discrepancies found along the analysis are of the order of 20%.

It is worthwhile now to compare the efficiency of the two methods in general. In the first place, one does not reveal any secret saying that CFD codes are computationally expensive. On the other hand, having said that the scale of the gradients is one particle diameter, one has served the trouble: Effectively, the cell size cannot be greater than a few particles. At values of the Mach number of about 10 in some phases of the motion, inertia is the most prominent mechanism of transport. Diffusion operates at very small length scales, and is of less importance than inertia, but plays a role in some other phases of the motion, when the typical Mach number drops below 1 in the dense phase, and cannot be just neglected. In addition, explicit time schemes like the one used in this paper introduce a stability condition which turns more and more restrictive as the diffusion length scales (the size of the particles) become smaller. The result is that for submillimetric particles, most commonly used in real experiments, the same problem treated here turns unbearably stiff, as the typical timescale of the pattern does not decrease in the same correspondence.

In any case one must resolve length scales of the typical size of one particle, and the ratio one cell \approx one particle is extremely unfavorable to computational hydrodynamics in terms of efficiency. Moreover, high resolution shock-capturing schemes like WENO add an extra cost in the computation which often amounts the largest portion of the total CPU time. There is some room for optimization though, in the sense that not everywhere, not all the time, such extraordinary effort to construct highly accurate numerical fluxes should be necessary, and thus the simulation time could this way be reduced.

The question about boundary conditions still deserves an additional remark. Here the most simple choice has been made, with specular reflecting boundaries without any portion of no-slip in the tangential direction (the velocity component parallel to the plate is not disturbed by the boundary). Presumably, in order to mimic rough particles some partial slip would have to be introduced with parameters to be determined from MD simulations, although friction may trigger rotational mechanisms which are not contemplated in the set of hydrodynamic equations considered here.

Finally, one should ask why the agreement between molecular dynamics and hydrodynamics is here so good, so robust, when all ingredients are present to make it fail. At high densities collisions are not binary, fluxes are thus nonlocal and the expressions for the kinetic coefficients should no longer apply, not to mention the degree of inelasticity (the restitution is only $e = 0.75$) which invalidates the assumption of small gradients on which all kinetic theory expansions are based. It seems that there is only one reason which can explain the agreement: The dynamics is mostly Eulerian and details like constitutive relations and transport coefficients are not definitive. So much so that in practice, if one focuses the attention on modeling accurately the shock wave and introduces a sensible equation of state, the instability is “easily” reproduced, as in molecular dynamics, with the essential contribution of inelasticity.

JAC acknowledges the support from DGI-MEC (Spain) project MTM2005-08024. The research of TP was supported by a Grant from the G.I.F., the German-Israeli Foundation

for Scientific Research and Development. CS thanks support from project MEC:DPI2003-06725-C02-01 of the Spanish Ministry of Education and Science.

Appendix A. Formulas for local variables

Here, we summarize the formulas for the explicit eigenvalues and eigenvectors of the Jacobian matrix of the Euler part of (3.1) in 2D, for general equations of state depending on the density and the enthalpy. As discussed in Section 3, the system (3.1) can be rewritten as

$$\frac{\partial \mathbf{u}}{\partial t} + \frac{\partial}{\partial x_1} \mathbf{f}(\mathbf{u}) + \frac{\partial}{\partial x_2} \mathbf{g}(\mathbf{u}) = \mathbf{S}(\mathbf{u}) \quad (\text{A } 1)$$

with obvious definitions for $\mathbf{f}(\mathbf{u})$, $\mathbf{g}(\mathbf{u})$ and $\mathbf{S}(\mathbf{u})$ and with the vector $\mathbf{u} = (u_1, u_2, u_3, u_4)$ whose components are given by

$$\begin{aligned} u_1 &= \rho \\ u_2 &= \rho U_1 \\ u_3 &= \rho U_2 \\ u_4 &= \rho \epsilon + \frac{1}{2} \rho |\mathbf{U}|^2 = \rho \epsilon + \frac{1}{2} \rho (U_1^2 + U_2^2) . \end{aligned} \quad (\text{A } 2)$$

The components of f are

$$\begin{aligned} f_1(\mathbf{u}) &= u_2 & , & & f_2(\mathbf{u}) &= p + \frac{u_2^2}{u_1} \\ f_3(\mathbf{u}) &= \frac{u_2 u_3}{u_1} & , & & f_4(\mathbf{u}) &= \frac{u_2}{u_1} (p + u_4) \end{aligned} \quad (\text{A } 3)$$

where the pressure is assumed to be a function of density and enthalpy,

$$p = p(\rho, \epsilon) = p\left(u_1, \frac{u_3}{u_1} - \frac{1}{2} \frac{u_2^2}{u_1}\right) . \quad (\text{A } 4)$$

The sound speed is given by

$$c_s^2 = \frac{\partial p}{\partial \rho} + \frac{p}{\rho^2} \frac{\partial p}{\partial \epsilon} = p_\rho + \frac{p}{\rho^2} p_\epsilon, \quad (\text{A } 5)$$

Given the auxiliary function is now $H = (p + u_4)/u_1$, the eigenvalues of the Jacobian matrix $\mathbf{f}'(\mathbf{u})$ are given by

$$\Lambda_- = \frac{u_2}{u_1} - c_s \quad , \quad \Lambda_2 = \Lambda_3 = \frac{u_2}{u_1} \quad \text{and} \quad \Lambda_+ = \frac{u_2}{u_1} + c_s \quad (\text{A } 6)$$

and their corresponding right and left eigenvectors are

$$r_\pm = \begin{pmatrix} 1 \\ \frac{u_2}{u_1} \pm c_s \\ \frac{u_3}{u_1} \\ H \pm \frac{u_2}{u_1} c_s \end{pmatrix} \quad r_2 = \begin{pmatrix} 1 \\ \frac{u_2}{u_1} \\ \frac{u_3}{u_1} \\ H - \frac{1}{b_1} \end{pmatrix} \quad r_3 = \begin{pmatrix} 0 \\ 0 \\ 1 \\ \frac{u_3}{u_1} \end{pmatrix} \quad (\text{A } 7)$$

and

$$l_{\pm} = \begin{pmatrix} \frac{1}{2} \mp \frac{u_2}{u_1} \frac{1}{2c_s} + \frac{b_1}{2} \left(\frac{u_2^2 + u_3^2}{u_1^2} - H \right) \\ -\frac{b_1}{2} \frac{u_2}{u_1} \pm \frac{1}{2c_s} \\ -\frac{b_1}{2} \frac{u_3}{u_1} \\ \frac{b_1}{2} \end{pmatrix}; \quad l_2 = \begin{pmatrix} \left[H - \frac{u_2^2}{u_1^2} - \frac{u_3^2}{u_1^2} \right] b_1 \\ \frac{u_2}{u_1} b_1 \\ \frac{u_3}{u_1} b_1 \\ -b_1 \end{pmatrix}; \quad l_3 = \begin{pmatrix} -\frac{u_3}{u_1} \\ 0 \\ 1 \\ 0 \end{pmatrix} \quad (\text{A } 8)$$

respectively, where $b_1 = p_{\epsilon} / \rho c_s^2$. For the fluxes associated with the x_2 -derivative, that is,

$$\begin{aligned} g_1(\mathbf{u}) &= u_3 & , & \quad g_2(\mathbf{u}) = \frac{u_2 u_3}{u_1} \\ g_3(\mathbf{u}) &= p + \frac{u_3^2}{u_1} & , & \quad g_4(\mathbf{u}) = \frac{u_3}{u_1} (p + u_4); \end{aligned} \quad (\text{A } 9)$$

we just need to swap indices 2 and 3 in all formulas above, and the second and third components in all right and left eigenvectors.

REFERENCES

- SUPPLEMENTARY MATERIAL Animated sequences are available as supplementary material. see <http://www.etseq.urv.es/personal/csalue/movies>
- AOKI, K. M. & AKIYAMA, T. 1996 Spontaneous wave pattern formation in vibrated granular materials. *Phys. Rev. Lett.* **77**, 4166–4169.
- AOKI, K. M. & AKIYAMA, T. 1997 Reply on Bizon *et al.* (1997). *Phys. Rev. Lett.* **79**, 4714.
- BIZON, C., SHATTUCK, M. D., NEWMAN, J. T., UMBANHOWAR, P. B., SWIFT, J. B., MCCORMICK, W. D. & SWINNEY, H. L. 1997 Comment on Aoki & Akiyama (1996). *Phys. Rev. Lett.* **79**, 4713.
- BIZON, C., SHATTUCK, M. D. & SWIFT, J. B. 1999 Linear stability analysis of a vertically oscillated granular layer. *Phys Rev E Stat Phys Plasmas Fluids Relat Interdiscip Topics* **60**, 7210.
- BOBYLEV, A. V., CARRILLO, J. A. & GAMBA, I. M. 2000 On some properties of kinetic and hydrodynamic equations for inelastic interactions. *J. Stat. Phys.* **98** (3-4), 743–773.
- BOUGIE, J., KREFT, J., SWIFT, J. B. & SWINNEY, H. 2005 Onset of patterns in an oscillated granular layer: continuum and molecular dynamics simulations. *Phys. Rev. E* **71**, 021301.
- BOUGIE, J., MOON, S. J., SWIFT, J. & SWINNEY, H. 2002 Shocks in vertically oscillated granular layers. *Phys. Rev. E* **66**, 051301.
- BRILLIANTOV, N. V. & PÖSCHEL, T. 2004 *Kinetic Theory of Granular Gases*. Oxford: Oxford University Press.
- BRILLIANTOV, N. V., SALUEÑA, C., SCHWAGER, T. & PÖSCHEL, T. 2004 Transient structures in a granular gas. *Phys. Rev. Lett.* **93**, 134301.
- BRILLIANTOV, N. V., SPAHN, F., HERTZSCH, J.-M. & PÖSCHEL, T. 1996 A model for collisions in granular gases. *Phys. Rev. E* **53**, 5382.
- CLÉMENT, E., VANEL, L., RAJCHENBACH, J. & DURAN, J. 1996 Pattern formation in a vibrated 2d granular layer. *Phys. Rev. E* **53**, 2972–2975.
- VAN DOORN, E. & BEHRINGER, R. P. 1997 Onset and evolution of a wavy instability in shaken sand. *Phys. Lett. A* **235**, 469.
- DOUADY, S., FAUVE, S. & LAROCHE, C. 1989 Subharmonic instabilities and defects in a granular layer under vertical vibrations. *Europhys. Lett.* **8**, 621–627.
- FARADAY, M. 1831 On a peculiar class of acoustical figure and on certain forms assumed by groups of particles upon vibrating elastic surfaces. *Phil. Trans. R. Soc. Lond.* **121**, 299.
- GARZÓ, V. & DUFTY, J. W. 1999 Dense fluid transport for inelastic hard spheres. *Phys. Rev. E* **59**, 5895–5911.
- GOLDHIRSCH, I. 1999 Scales and kinetics of granular flows. *Chaos* **9**, 659–672.

- GOLDHIRSCH, I. 2001 Probing the boundaries of hydrodynamics. In *Granular Gases* (ed. T. Pöschel & S. Luding), *Lecture Notes in Physics*, vol. 564, pp. 79–99. Berlin: Springer.
- GOLDHIRSCH, I. 2003 Rapid granular flows. *Ann. Rev. Fluid Mech.* **35**, 267.
- GOLDSHTEIN, A. & SHAPIRO, M. 1995 Mechanics of collisional motion of granular materials. Part 1: General hydrodynamic equations. *J. Fluid Mech.* **282**, 75.
- HILL, S. A. & MAZENKO, G. F. 2003 Granular clustering in a hydrodynamic simulation. *Phys. Rev. E* **67**, 061302.
- JENKINS, J. & RICHMAN, M. W. 1985*a* Grad’s 13-moment system for a dense gas of inelastic spheres. *Arch. Rational Mech. Anal.* **87**, 355.
- JENKINS, J. & RICHMAN, M. W. 1985*b* Kinetic theory for plane flows of a dense gas of identical, rough, inelastic, circular disks. *Phys. Fluids* **28**, 3485.
- JIANG, G. & SHU, C.-W. 1996 Efficient implementation of weighted eno schemes. *J. Comput. Phys.* **126**, 202.
- KAMENETSKY, V., GOLDSHTEIN, A., SHAPIRO, M. & DEGANI, D. 2000 Evolution of a shock wave in a granular gas. *Phys. Fluids* **12** (11), 3036–3049.
- LUDING, S. 1997 Surface waves and pattern formation in vibrated granular media. In *Powders and Grains’97* (ed. R. P. Behringer & J. T. Jenkins), p. 373. Rotterdam: Balkema.
- LUDING, S., CLÉMENT, E., RAJCHENBACH, J. & DURAN, J. 1996 Simulations of pattern formation in vibrated granular media. *Europhys. Lett.* **36**, 247–252.
- LUDING, S. & MCNAMARA, S. 1998 How to handle the inelastic collapse of a dissipative hard-sphere gas with the TC model. *Granular Matter* **1**, 113–128.
- LUTSKO, J. F. 2005 Transport properties of dense dissipative hard-sphere fluids for arbitrary energy loss models. *Phys. Rev. E* **72**, 021306.
- MCNAMARA, S. & YOUNG, W. R. 1993 Inelastic collapse in two dimensions. *Phys. Rev. E* **50**, R28–R31.
- MEERSON, B., PÖSCHEL, T. & BROMBERG, Y. 2003 Close-packed floating clusters: Granular hydrodynamics beyond the freezing point? *Phys. Rev. Lett.* **91**, 24301.
- MEERSON, B., PÖSCHEL, T., SASOROV, P. V. & SCHWAGER, T. 2004 Giant fluctuations at a granular phase separation threshold. *Phys. Rev. E* **69**, 21302.
- MELO, F., UMBANHOWAR, P. & SWINNEY, H. L. 1994 Transition to parametric wave patterns in a vertically oscillated granular layer. *Phys. Rev. Lett.* **72**, 172–175.
- MELO, F., UMBANHOWAR, P. & SWINNEY, H. L. 1995 Hexagons, kinks, and disorder in oscillated granular layers. *Phys. Rev. Lett.* **75**, 3838–3841.
- METCALFE, T., KNIGHT, J. B. & JAEGER, H. M. 1997 Surface patterns in shallow beds of vibrated granular material. *Physica A* **236**, 202–210.
- PAK, H. K. & BEHRINGER, R. P. 1993 Surface waves in vertically vibrated granular materials. *Phys. Rev. Lett.* **71**, 1832.
- PÖSCHEL, T. & SCHWAGER, T. 2005 *Computational Granular Dynamics*. Berlin: Springer.
- PÖSCHEL, T., SCHWAGER, T. & SALUENA, C. 2000 Onset of fluidization in vertically shaken granular material. *Phys. Rev. E* **62**, 1361.
- RAMÍREZ, R., PÖSCHEL, T., BRILLIANTOV, N. V. & SCHWAGER, T. 1999 Coefficient of restitution of colliding viscoelastic spheres. *Phys. Rev. E* **60**, 4465–4472.
- RENARD, S., SCHWAGER, T., PÖSCHEL, T. & SALUENA, C. 2001 Vertically shaken column of spheres. onset of fluidization. *Eur. Phys. J. E* **4**, 233.
- RERICHA, E., BIZON, C., SHATTUCK, M. & SWINNEY, H. 2002 Shocks in supersonic sand. *Phys. Rev. Lett.* **88**, 1.
- ROTHMAN, D. H. 1998 Oscillons, spiral waves, and stripes in a model of vibrated sand. *Phys. Rev. E* **57**, R1239–R1242.
- SCHWAGER, T. & PÖSCHEL, T. 1998 Coefficient of restitution of viscous particles and cooling rate of granular gases. *Phys. Rev. E* **57**, 650–654.
- SHATTUCK, M. 2005 New boundary conditions for granular fluids. *Personal communication*.
- SHU, C.-W. 1998 Essentially non-oscillatory and weighted essentially non-oscillatory schemes for hyperbolic conservation laws. In *Advanced Numerical Approximation of Nonlinear Hyperbolic Equations* (ed. A. Quarteroni), *Lecture Notes in Mathematics*, vol. 1697, p. 325. Berlin: Springer.
- SHU, C.-W. & OSHER, S. 1998 Efficient implementation of essentially non-oscillatory shock capturing schemes. *J. Comput. Phys.* **77**, 439.

- TORQUATO, S. 1995 Nearest-neighbor statistics for packings of hard spheres and disks. *Phys. Rev. E* **51**, 3170.
- TSIMRING, L. S. & ARANSON, I. S. 1997 Localized and cellular patterns in a vibrated granular layer. *Phys. Rev. Lett.* **79**, 213–216.
- UMBANHOWAR, P. B., MELO, F. & SWINNEY, H. L. 1996 Localized excitations in a vertically vibrated granular layer. *Nature* **382**, 793–796.
- UMBANHOWAR, P. B., MELO, F. & SWINNEY, H. L. 1998 Periodic, aperiodic, and transient patterns in vibrated granular layers. *Physica A* **249**, 1–9.
- WASSGREN, C. R., BRENNEN, C. E. & HUNT, M. L. 1996 Vertical vibration of a deep bed of granular material in a container. *J. Appl. Mech.* **63**, 712–719.